

Article

Poly(*bis*[2-(methacryloyloxy)ethyl] phosphate)/Bacterial Cellulose Nanocomposites: Preparation, Characterization and Application as Polymer Electrolyte Membranes

Carla Vilela ^{1,*} , Ana P. C. Martins ¹, Nuno Sousa ², Armando J. D. Silvestre ¹ ,
Filipe M. L. Figueiredo ²  and Carmen S. R. Freire ¹

¹ Department of Chemistry, CICECO-Aveiro Institute of Materials, University of Aveiro, 3810-193 Aveiro, Portugal; apcm@ua.pt (A.P.C.M.); armsil@ua.pt (A.J.D.S.); cfreire@ua.pt (C.S.R.F.)

² Department of Materials and Ceramic Engineering, CICECO-Aveiro Institute of Materials, University of Aveiro, 3810-193 Aveiro, Portugal; nunoasousa@ua.pt (N.S.); lebre@ua.pt (F.M.L.F.)

* Correspondence: cvilela@ua.pt; Tel.: +351-234-370-200

Received: 18 June 2018; Accepted: 10 July 2018; Published: 14 July 2018



Abstract: Recent studies have demonstrated the potential of bacterial cellulose (BC) as a substrate for the design of bio-based ion exchange membranes with an excellent combination of conductive and mechanical properties for application in devices entailing functional ion conducting elements. In this context, the present study aims at fabricating polyelectrolyte nanocomposite membranes based on poly(*bis*[2-(methacryloyloxy)ethyl] phosphate) [P(*bis*MEP)] and BC via the in-situ free radical polymerization of *bis*[2-(methacryloyloxy)ethyl] phosphate (*bis*MEP) inside the BC three-dimensional network under eco-friendly reaction conditions. The resulting polyelectrolyte nanocomposites exhibit thermal stability up to 200 °C, good mechanical performance (Young's modulus > 2 GPa), water-uptake ability (79–155%) and ion exchange capacity ($[H^+] = 1.1\text{--}3.0 \text{ mmol g}^{-1}$). Furthermore, a maximum protonic conductivity of ca. 0.03 S cm^{-1} was observed for the membrane with P(*bis*MEP)/BC of 1:1 in weight, at 80 °C and 98% relative humidity. The use of a bifunctional monomer that obviates the need of using a cross-linker to retain the polyelectrolyte inside the BC network is the main contribution of this study, thus opening alternative routes for the development of bio-based polyelectrolyte membranes for application in e.g., fuel cells and other devices based on proton separators.

Keywords: bacterial cellulose; proton exchange membrane; nanocomposites; poly(*bis*[2-(methacryloyloxy)ethyl] phosphate); protonic conductivity

1. Introduction

The most abundant natural polymer on earth, viz. cellulose, is continuously scoring points in all domains of research particularly on the development of multifunctional materials [1–3]. In fact, the versatility of cellulose is even fostered when its nanoscale forms are considered, namely cellulose nanofibrils (CNFs), cellulose nanocrystals (CNCs) and bacterial cellulose (BC), whose interest for the design of innovative and all-purpose nanomaterials has skyrocketed during the last couple of years, including in the nanocomposites domain [4–9]. Within the nanoscale forms of cellulose, BC has a huge advantage in terms of mechanical performance and dimensional stability, apart from its inherent biodegradability, biocompatibility and high water-holding capacity [10,11]. The most salient feature of BC is associated with its moldability during biosynthesis and shape retention, as well as with the recently achieved degree of control over the three-dimensional morphology of BC films across

several length scales [12] that enables the design of materials with engineerable size and form for myriad applications.

The synergetic combination of the ultrafine nanofibrous network of BC with a proton or anion conducting phase has proven its viability for application as partially bio-based platform in the fabrication of ion conducting membranes for polymer electrolyte fuel cells (PEFCs) [13–25]. Practical applicable proton- or anion-exchange membranes derived from BC can satisfy the strict requirements for application as separators in PEFCs, namely conductivity, suitable mechanical performance, gas tightness, dimensional and chemical stability under oxidative environment, and variable temperature and humidity conditions [26,27]. The fabrication of these BC-based membrane separators can be performed following different strategies like for example the in-situ deposition of metallic nanoparticles on BC membranes [13,14], the diffusion of an ion conductor onto the BC membrane network [18,22], blending of BC dispersed nanofibers with a polyelectrolyte or ionomer followed by casting [25], modification of BC via grafting polymerization with an electrolyte [19], the in-situ polymerization of electrolyte monomers within the pure BC three-dimensional network [20,21,24], and by chemical modification of the BC template [15,16].

Following our ongoing interest in bio-based ion separator materials for application in PEFCs [20–24], this study reports the fabrication of polyelectrolyte membranes through the exploitation of a mono-acidic phosphate bearing polymer containing two polymerizable methacryloyl moieties, i.e., poly(*bis*[2-(methacryloyloxy)ethyl] phosphate) [P(*bis*MEP)], and BC. The key aspect differentiating these membranes from polymer electrolyte membranes (PEMs) reported in literature is the use of a bifunctional monomer that obviates the need of using a cross-linker to retain the polyelectrolyte inside the BC network, and modulate the properties of the ensuing proton separator material.

2. Materials and Methods

2.1. Chemicals and Materials

2-Azobis(2-methylpropionamide) dihydrochloride (AAPH, 97%) and *bis*[2-(methacryloyloxy)ethyl] phosphate (*bis*MEP, ≥99%) were supplied by Sigma-Aldrich (Saint Louis, MO, USA) and used as received without any further purification. Other reagents and solvents were of laboratory grade. Bacterial cellulose (BC) was biosynthesized in our laboratory in the form of wet membranes by the *Gluconacetobacter sacchari* bacterial strain [28].

2.2. Preparation of P(*bis*MEP)/BC Nanocomposite Membranes

The P(*bis*MEP)/BC nanocomposite membranes were prepared following an established procedure based on the in-situ free radical polymerization of a monomer inside the BC three-dimensional porous network [24]. In brief, never-dried BC membranes with ca. 40% water content (400 mg dry weight) were placed in Erlenmeyers stoppered with rubber septa and purged with nitrogen. At the same time, aqueous solutions of monomer (*bis*MEP) and radical initiator (AAPH, 2.0% *w/w* relative to the monomer) were prepared according to Table 1 and transferred to the Erlenmeyers containing the drained BC membranes. After the total incorporation of the solutions into the BC membranes during 1 h in ice, the reaction mixtures were placed in an oil bath at 70 °C for 6 h. The nanocomposite membranes were then thoroughly washed with distilled water and dried at 40 °C in a ventilated oven for 12 h. The experiments were performed in triplicate and the samples analyzed as thin dried membranes. For comparison purposes, P(*bis*MEP) homopolymer was prepared in the absence of BC.

Table 1. List of the membranes with the corresponding weight compositions and thickness; BC: bacterial cellulose, P(*bis*MEP): poly(*bis*[2-(methacryloyloxy)ethyl] phosphate).

Membranes	Nominal Composition ^a	Measured Composition ^b			Thickness/ μm
	$W_{\text{bisMEP}}/W_{\text{BC}}$	$W_{\text{P(bisMEP)}}/W_{\text{BC}}$	$W_{\text{BC}}/W_{\text{total}}$	$W_{\text{P(bisMEP)}}/W_{\text{total}}$	
BC	–	–	1.0	–	42 \pm 11
P(<i>bis</i> MEP)/BC_1	3	0.26	0.79	0.21	64 \pm 11
P(<i>bis</i> MEP)/BC_2	5	1.0	0.50	0.50	132 \pm 12

^a The nominal composition was determined by considering the initial weight of *bis*MEP monomer (W_{bisMEP}) and BC (W_{BC}) that were utilized for the in-situ free radical polymerization; ^b The measured composition was calculated by taking into account the weight of the nanocomposite membrane (W_{total}), BC (W_{BC}) and P(*bis*MEP) homopolymer ($W_{\text{P(bisMEP)}} = W_{\text{total}} - W_{\text{BC}}$).

2.3. Characterization Methods

The thickness of the membranes was measured by a hand-held digital micrometre (Mitutoyo Corporation (Kawasaki, Japan)) with an accuracy of 0.001 mm. All measurements were randomly performed at different sites of the membranes and the mean value was recorded.

Attenuated total reflection-Fourier transform Infrared (ATR-FTIR) spectra were recorded with a Perkin-Elmer FT-IR System Spectrum BX spectrophotometer equipped with a single horizontal Golden Gate ATR cell, over the range of 600–4000 cm^{-1} at a resolution of 4 cm^{-1} over 32 scans.

Solid-state carbon cross-polarization/magic-angle-spinning nuclear magnetic resonance (^{13}C CP/MAS NMR) spectra were collected on a Bruker Avance III 400 spectrometer operating at a B0 field of 9.4 T using 9 kHz MAS with proton 90° pulse of 3 μs , time between scans of 3 s, and a contact time of 2000 μs . ^{13}C chemical shifts were referenced to glycine (C=O at δ 176 ppm).

The X-ray diffraction (XRD) was performed on a Phillips X'pert MPD diffractometer using Cu $K\alpha$ radiation ($\lambda = 1.541 \text{ \AA}$) with a scan rate of $0.05^\circ \text{ s}^{-1}$. The XRD patterns were collected in reflection mode with the membranes placed on a Si wafer (negligible background signal) for mechanical support and thus avoid sample bending.

Scanning electron microscopy (SEM) images of the surface and cross-section of the membranes were obtained by a HR-FESEM SU-70 Hitachi microscope operating at 4 kV. The microscope was equipped with an energy dispersive X-ray spectroscopy (EDS) Bruker QUANTAX 400 detector for elemental analysis. The membranes were previously coated with a carbon film.

Thermogravimetric analysis (TGA) was carried out with a SETSYS Setaram TGA analyser equipped with a platinum cell. The samples were heated from room temperature (RT) to 800 $^\circ\text{C}$ at a constant rate of 10 $^\circ\text{C min}^{-1}$ under a nitrogen atmosphere (200 mL min^{-1}).

Tensile tests were performed on a uniaxial Instron 5564 testing machine in the traction mode at a cross-head velocity of 10 mm min^{-1} using a 500 N static load cell. The specimens were rectangular strips ($50 \times 10 \text{ mm}^2$) previously dried at 40 $^\circ\text{C}$ and equilibrated at RT in a 50% relative humidity (RH) atmosphere prior to testing. All measurements were performed on 5 replicates and the results were expressed as the average value.

The water-uptake (WU) was determined via immersion of specimens with $1 \times 1 \text{ cm}^2$ in distilled water at RT for 48 h. After removing the membranes out of the water, the wet surfaces were dried in filter paper, and the wet weight (W_w) was measured. The WU is calculated by the equation: $WU (\%) = [(W_w - W_0)/W_0]$, where W_0 is the initial weight of the dry membrane.

Ion exchange capacity (IEC) measurements were carried out by soaking the samples in an aqueous solution of NaCl (0.1 M) for 24 h at RT, followed by titration with an aqueous solution of NaOH (0.005 M). The IEC was assessed by the equation: $\text{IEC (mmol g}^{-1}\text{)} = (V_{\text{NaOH}} \times M_{\text{NaOH}})/W_0$, where V_{NaOH} is the volume (in mL) of the NaOH aqueous solution at the equivalence point, and M_{NaOH} is the molar concentration of the NaOH aqueous solution.

Electrochemical impedance spectroscopy (Agilent (County of Santa Clara, CA, USA) E4980A Precision LCR meter) was used to determine the in-plane protonic conductivity (σ) under variable

temperature (40 °C to 94 °C) and RH (30% to 98%) conditions in an ACS Discovery DY110 climatic chamber. The measurements were performed on rectangular membrane specimens with dimensions of $\sim 1.5 \times 0.5 \text{ cm}^2$ on which two stripes of silver (Agar Scientific (Essex, UK) silver paste) were painted separated by ca. 1 cm. Furthermore, a pseudo 4-electrode configuration in a tubular sample holder was used to ensure full exposure of the membrane surface to the controlled atmosphere and provide the necessary electrical contact between the sample and the LCR meter. The impedance spectra were recorded between 20 Hz and 2×10^6 Hz with test signal amplitude of 100 mV, and analysed with the ZView software (Version 2.6b, Scribner Associates (Southern Pines, NC, USA)) to evaluate the Ohmic resistance (R) of the membrane. The conductivity was then calculated using the equation: $\sigma = L_0(R\delta w)^{-1}$, where L_0 is the distance between the two silver stripes, and δ and w are the thickness and width of the membrane, respectively.

3. Results and Discussion

In this study, two distinct nanocomposite membranes based on P(*bis*MEP) and BC were produced via in-situ free radical polymerization of the respective phosphate ester bearing monomer, i.e., *bis*MEP, inside the BC three-dimensional network under eco-friendly reaction conditions, namely innocuous solvent (water) and low reaction temperature. The selection of this mono-acidic phosphate monomer was based on: (i) the lower acidity of the phosphoric acid groups when compared e.g., to sulfonic acid groups, which expectedly translates into membranes with higher thermal-oxidative stability [21,29]; (ii) the bifunctionality of the monomer that precludes the use of a cross-linker to efficiently retain the polyelectrolyte inside the BC network; and (iii) its demonstrated potential for application as polymeric cation-exchange monoliths for capillary liquid chromatography [30] and cation exchange membranes for blocking complexing ions in presence of non-complexing ions [31].

Overall, the nanocomposite membranes P(*bis*MEP)/BC_1 and P(*bis*MEP)/BC_2 were very homogeneous with no noticeable irregularities on both surfaces of the membranes as illustrated in Figure 1, which is indicative of a good dispersion of P(*bis*MEP) inside the BC network. Furthermore, the thickness of the membranes increased from $42 \pm 11 \text{ }\mu\text{m}$ for pure BC to $64 \pm 11 \text{ }\mu\text{m}$ for P(*bis*MEP)/BC_1 and $132 \pm 12 \text{ }\mu\text{m}$ for P(*bis*MEP)/BC_2 (Table 1).



Figure 1. Visual aspect of a dry pure BC (bacterial cellulose) membrane, and P(*bis*MEP)/BC_1 and P(*bis*MEP)/BC_2 nanocomposites.

3.1. Structural and Morphological Characterization

The successful inclusion of P(*bis*MEP) inside the BC network was demonstrated by ATR-FTIR spectroscopy. The infrared spectra of P(*bis*MEP), pure BC, and P(*bis*MEP)/BC_1 and P(*bis*MEP)/BC_2 nanocomposites are shown in Figure 2. The ATR-FTIR spectrum of P(*bis*MEP) shows all the relevant bands at 1714 cm^{-1} (C=O stretching), 1159 cm^{-1} (C–O stretching), 1054 cm^{-1} (P=O_(hydrogen bonded) stretching) and 976 cm^{-1} (P–O–C stretching) [32]. The ATR-FTIR spectrum of BC displays the characteristic absorption bands of cellulose at 3340 cm^{-1} (O–H stretching), 2900 cm^{-1} (C–H stretching), 1310 cm^{-1} (O–H bending) and 1030 cm^{-1} (C–O stretching) [33]. Regarding the P(*bis*MEP)-based nanocomposites, their spectra clearly bear a resemblance to the sum of the vibration peaks of the corresponding individual components. Besides, the nonappearance of the band at about 1635 cm^{-1} corresponding to the C=C double bond stretching of the methacrylic group of the monomer [32,34], supports the occurrence of the in-situ free radical polymerization of *bis*MEP.

Furthermore, the augment of the intensity of the bands assigned to the polyelectrolyte agrees with the weight-gain ($W_{P(bisMEP)}/W_{BC}$) determined for the nanocomposites (Table 1).

The solid-state ^{13}C CP/MAS NMR spectroscopy also validated the composition of the nanocomposites through the presence of the representative resonances of both $P(bisMEP)$ and BC, as depicted in Figure 3. Nanocomposites $P(bisMEP)/BC_1$ and $P(bisMEP)/BC_2$ exhibit the resonances of the BC at δ 65.2 ppm (C6), 71.7–74.5 ppm (C2, C3, C5), 89.0 ppm (C4) and 105.1 ppm (C1) [35], jointly with those of $P(bisMEP)$ at δ 16.5 ppm (CH_3 of polymer backbone, C3'), 45.0 ppm (quaternary C of polymer backbone, C2'), 54.4 ppm (CH_2 of polymer backbone, C1'), 65.1 ppm (OCH_2CH_2O , C5') and 177.2 ppm (C=O, C4'). The comparison between the spectra of $P(bisMEP)/BC_1$ and $P(bisMEP)/BC_2$ shows an increase of the intensity of the resonances allocated to $P(bisMEP)$ with the increasing polymer content and are in accord with the $W_{P(bisMEP)}/W_{total}$ ratio (Table 1). The absence of the carbon resonances associated with the two double bonds (C=C) of the methacryloyl moiety of the monomer, is an additional evidence of the occurrence of the in-situ polymerization of $bisMEP$, as formerly shown by ATR-FTIR.

The effect of the inclusion of $P(bisMEP)$ within the nanocomposite three-dimensional network on the crystallinity of BC was assessed by XRD (Figure 4). $P(bisMEP)$ exhibits a diffraction profile characteristic of amorphous polymeric materials, while the diffraction pattern of BC perfectly shows the three main characteristic reflections of cellulose I (native cellulose) at 2θ values of about 14.5° , 16.6° and 22.6° associated with the (100), (010) and (110) crystallographic planes [36]. The XRD diffractograms of the membranes display the main features of cellulose but the intensity of the peaks at ca. 2θ 14.5° and 16.6° decreased relatively to the (110) crystallographic plane especially in the case of $P(bisMEP)/BC_2$ with 50 wt % of $P(bisMEP)$, which might be an indication of higher disorder in the inter-sheet spacing with the addition of the amorphous polymer [37]. An analogous behavior was reported for nanocomposite membranes of a poly(ionic liquid) with BC [24].

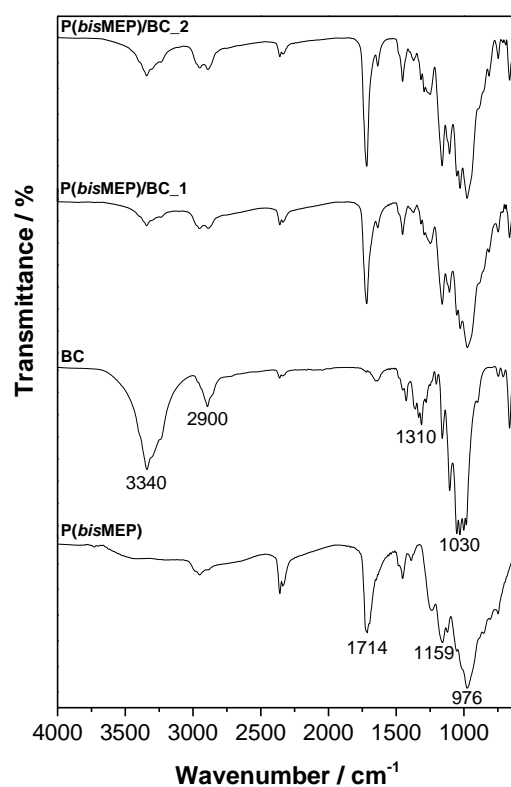


Figure 2. ATR-FTIR spectra of $P(bisMEP)$, pure BC, and $P(bisMEP)/BC_1$ and $P(bisMEP)/BC_2$ nanocomposite membranes.

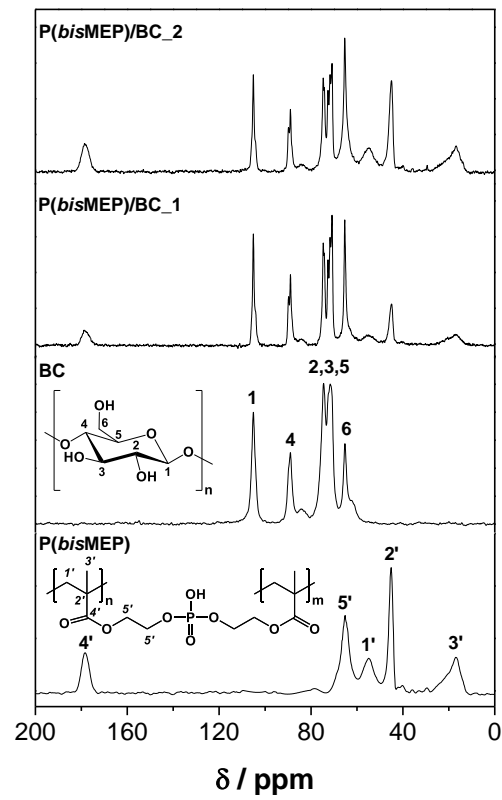


Figure 3. Solid-state ^{13}C CP/MAS NMR spectra of $\text{P}(\text{bisMEP})$, pure BC, and $\text{P}(\text{bisMEP})/\text{BC}_1$ and $\text{P}(\text{bisMEP})/\text{BC}_2$ nanocomposite membranes.

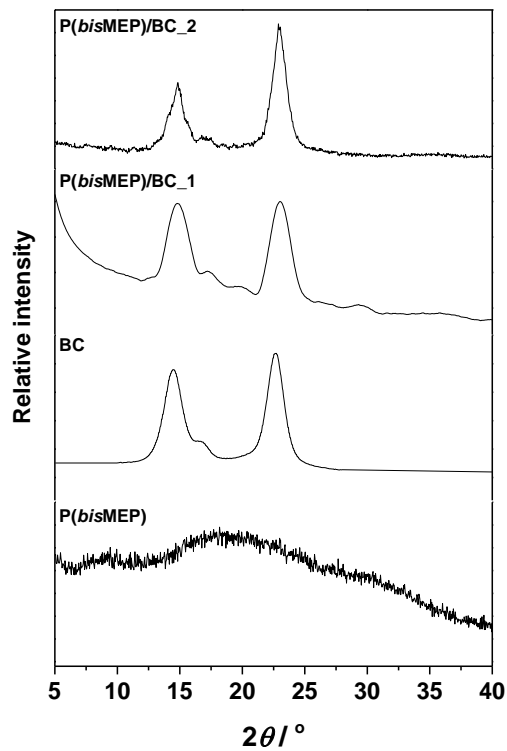


Figure 4. X-ray diffractograms of the $\text{P}(\text{bisMEP})$, pure BC, and $\text{P}(\text{bisMEP})/\text{BC}_1$ and $\text{P}(\text{bisMEP})/\text{BC}_2$ nanocomposite membranes.

Figure 5 displays the SEM images of the surface and cross-section of the two P(*bis*MEP)-based nanocomposites. Both membranes maintained the three-dimensional nanofibrillar network and lamellar microstructure representative of the BC morphology, particularly the P(*bis*MEP)/BC_1 nanocomposite that contains the higher BC content (79 wt %). So, these membranes present a highly anisotropic microstructure because of the alternating nanofibril layers of BC and the P(*bis*MEP) phase. This morphological anisotropy was recently demonstrated to originate differences in the protonic conductivity in the through- and in-plane configurations; nevertheless, the impact of this anisotropy in the fuel cell performance is lessened near RH saturated conditions, i.e., 98% RH [23].

The homogeneous distribution of P(*bis*MEP) inside the BC nanofibrous network was further corroborated by EDS analysis as illustrated in Figure 6. This technique certified the presence of phosphorus element as shown in the EDS spectrum (Figure 6c) of P(*bis*MEP)/BC_2, as well as the homogenous distribution of P(*bis*MEP) within the BC network as depicted in the SEM/EDS mapping of phosphorus element (Figure 6a,b, cross-section view) of the nanocomposite membrane containing 50 wt % of P(*bis*MEP).

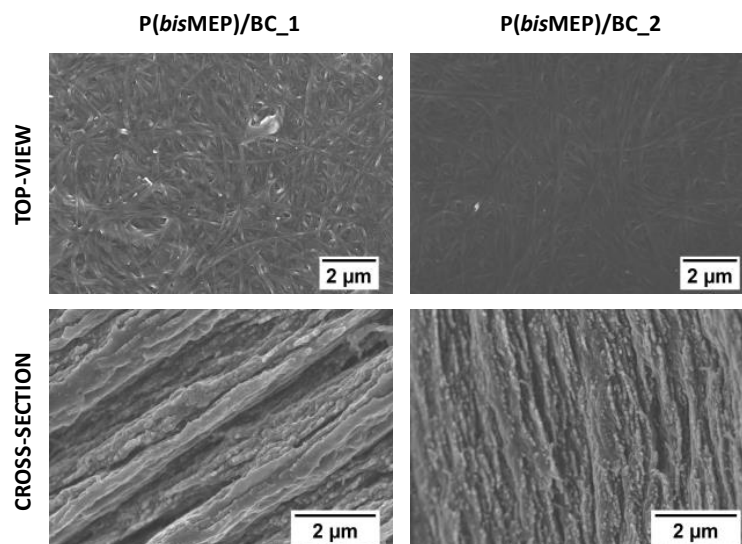


Figure 5. SEM images of the surface and cross-section of nanocomposite membranes.

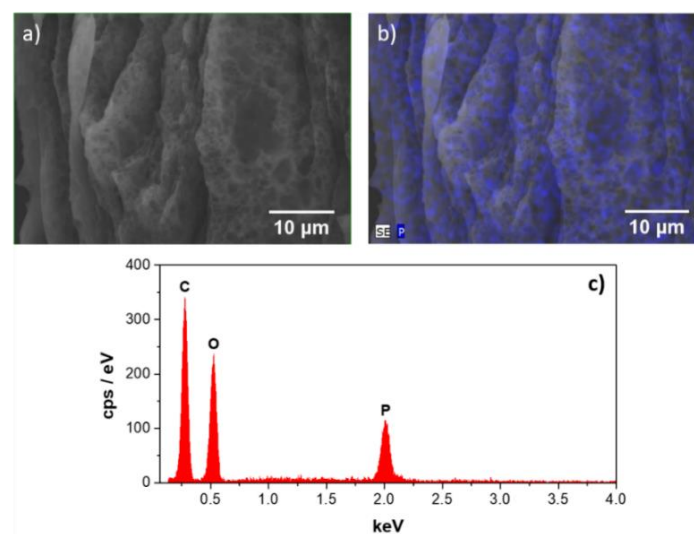


Figure 6. (a) SEM cross-sectional micrograph; (b) EDS map of phosphorus (P) element, and (c) EDS spectrum of nanocomposite membrane P(*bis*MEP)/BC_2.

3.2. Thermal Stability

The thermal stability and degradation profiles of the P(*bis*MEP)-based nanocomposites (and the corresponding individual components) were evaluated by thermogravimetric analysis under nitrogen atmosphere, and the data is summarized in Table 2. The P(*bis*MEP) homopolymer with a single weight-loss step degradation profile started to decompose close to 230 °C and reached a maximum decomposition temperature at about 304 °C, leaving a residue of ca. 40% at 800 °C almost certainly rich in phosphorus, in accordance with data reported elsewhere [38]. The TGA curve of pure BC, in addition to the dehydration below 100 °C (loss of ca. 5 wt %), showed a single-step degradation profile with initial and maximum decomposition temperatures at 266 °C and 347 °C, respectively, in good agreement with previously published data [21]. This single-step pathway is associated with the pyrolysis of the cellulose skeleton [39].

The TGA thermograms of the P(*bis*MEP)/BC nanocomposite membranes exhibit an intermediate behavior between the individual components with a two-step weight-loss degradation profile (Table 2). The first stage with maximum decomposition temperature (T_{dmax1}) of 234 °C for P(*bis*MEP)/BC_1 and 235 °C for P(*bis*MEP)/BC_2 is comparable to the degradation of the P(*bis*MEP) polymer backbone, whereas the second stage with maximum decomposition temperature (T_{dmax2}) of 300 °C for P(*bis*MEP)/BC_1 and 303 °C for P(*bis*MEP)/BC_2 corresponds to the degradation of the cellulose skeleton. This is corroborated by the fact that the magnitude of the loss at T_{dmax2} decreases with the reduction of the BC content. A weight-loss of about 60 wt % was obtained for P(*bis*MEP)/BC_1 and P(*bis*MEP)/BC_2 at temperatures up to 800 °C. Despite the reduction of the thermal stability of both nanocomposites in comparison with P(*bis*MEP) and BC, they are still thermally stable up to about 200 °C (loss of ca. 6 wt %), which is higher than the standard (<100 °C) and maximum (<140 °C) operating temperatures of the PEFCs technology [14,40]. Moreover, these results are comparable to those reported for BC-based membranes containing the cross-linked poly(methacryloyloxyethyl phosphate) (PMOEP) as the polyelectrolyte [21], which is the diprotic acid version of the P(*bis*MEP) homopolymer.

Table 2. TGA data of the P(*bis*MEP), BC and P(*bis*MEP)/BC nanocomposites.

Sample *	$T_{di}/^{\circ}\text{C}$	$T_{dmax1}/^{\circ}\text{C}$	$T_{dmax2}/^{\circ}\text{C}$
P(<i>bis</i> MEP)	230	289	–
BC	266	347	–
P(<i>bis</i> MEP)/BC_1	205	234	300
P(<i>bis</i> MEP)/BC_2	195	235	303

* See Table 1 for sample identification.

3.3. Mechanical Properties

The mechanical properties of P(*bis*MEP)/BC_1 and P(*bis*MEP)/BC_2 nanocomposites were evaluated by typical tensile tests and the results of Young's modulus, tensile strength and elongation at break are summarized in Table 3. Data for the P(*bis*MEP) homopolymer could not be obtained given its low film-forming ability. Regarding the pure BC membrane, the attained results showed a Young's modulus of 10.2 ± 2.21 GPa, tensile strength of 222 ± 47.0 MPa and elongation at break of $4.1 \pm 0.93\%$, which reach agreement with values reported in literature [41].

In the case of the nanocomposites, the Young's modulus and tensile strength increased with the increasing content of BC (50 wt % and 79 wt %), with the latter parameter experiencing a higher variation, particularly in the case of the nanocomposite containing 50 wt % of P(*bis*MEP). In fact, P(*bis*MEP)/BC_2 exhibits a tensile strength value of almost one order of magnitude lower than pure BC, whereas the Young's modulus is just four times inferior (Table 3). The impact is considerably lower in the case of the nanocomposite with 21 wt % polyelectrolyte (P(*bis*MEP)/BC_1), with the Young's modulus and the tensile strength attaining about 61% and 21.5% of the values of pure BC,

respectively. This outcome was expected given the superior mechanical performance of BC associated with the nanofibrils high aspect-ratio and highly ordered self-assembled nanostructure. The ultrafine nanofibrous network of pristine BC is indeed one of the major contributions of this biopolymer to the development of partially bio-based proton-exchange membranes for fuel cell applications. As an illustrative example of this feature, Yue and co-workers [15] functionalized BC with carboxylic moieties, which drastically reduced the tensile strength and modulus of the carboxymethylated-BC biopolymer to values of about 413 kPa and 814 kPa, respectively. Furthermore, the inclusion of polyaniline (conducting polymer) in a carboxymethylated-BC network further decreased the mechanical performance of the composite gel membranes [16]. Worth noting is the fact that these P(*bis*MEP)-based nanocomposite membranes present a better mechanical performance than Nafion® (the reference perfluorosulfonic acid membrane) in terms of Young's modulus (0.25 GPa) and tensile strength (43 MPa) [42].

On the other hand, the elongation at break of the nanocomposites is also lower when compared to the pure BC membrane (Table 3), probably due to a stronger constriction effect leading to an increase of the applied stress (with respect to the nominal stress) in the fracture region (with smaller cross-sectional area), going beyond the fracture point. In fact, the BC nanofibril network is known for exhibiting an auxetic behavior, i.e., negative Poisson ratio, for in-plane deformation [43]. This negative Poisson ratio implies that the network expands in the transverse direction when stretched [43–45]. The nanocomposite membranes are expected to display a conventional behavior with positive Poisson ratio, due to the fraction of P(*bis*MEP) and their lower crystallinity. The higher content of P(*bis*MEP) present in P(*bis*MEP)/BC_2 decreases the Young's modulus and tensile strength leading to a more elastic nanocomposite, in agreement with an elongation at break larger than for P(*bis*MEP)/BC_1.

Table 3. Tensile tests data: Young's modulus, tensile strength and elongation at break of the P(*bis*MEP)/BC nanocomposites.

Membrane *	Young's Modulus/GPa	Tensile Strength/MPa	Elongation at Break/%
BC	10.2 ± 2.21	222 ± 47.0	4.1 ± 0.93
P(<i>bis</i> MEP)/BC_1	6.22 ± 0.95	47.8 ± 9.4	0.68 ± 0.30
P(<i>bis</i> MEP)/BC_2	2.68 ± 0.41	23.5 ± 3.3	1.1 ± 0.24

* See Table 1 for membrane identification.

3.4. Water-Uptake and Ion Exchange Capacity

The water-uptake ability of the P(*bis*MEP)/BC nanocomposites was estimated by immersing the membranes in water during 48 h at room temperature. The *WU* data (Table 4) shows the increase of this parameter from 79 ± 6% to 155 ± 8% with the increasing content of P(*bis*MEP) from 21 wt % to 50 wt %. Such an increase is probably due to the increasing concentration of highly hygroscopic acid groups in P(*bis*MEP), which are likely to interact electrostatically with the adsorbed water molecules. One observes that the value obtained for P(*bis*MEP)/BC_1 is lower than the *WU* value of a pure BC membrane (121 ± 11%). The difference, although statistically significant with respect to the series of membranes prepared in this work, is within the natural dispersion of the water-uptake determined in previous works for BC. For example, and restricting to our own results, we have reported values of 100% [20,21] or even 165% [24]. Furthermore, both nanocomposites exhibit water-uptake values higher than those typically found for the commercial Nafion® ionomer (54%) [46], but lower than the corresponding values obtained for the cross-linked PMOEP/BC membranes prepared in our previous study [21].

Table 4 also displays the IEC of the P(*bis*MEP)/BC nanocomposite membranes. This data demonstrate that IEC increased from 1.1 ± 0.12 mmol g⁻¹ to 3.0 ± 0.05 mmol g⁻¹ with the augment of P(*bis*MEP) content from 21 wt % to 50 wt % (P(*bis*MEP)/BC_1 and P(*bis*MEP)/BC_2, respectively). Regardless of the null IEC value of BC due to the absence of ionic groups, the results obtained for the nanocomposite membranes were expectable given the electrolytic nature of P(*bis*MEP) exhibiting

an IEC of $3.5 \pm 0.02 \text{ mmol g}^{-1}$. The P(*bis*MEP)/BC_2 nanocomposite membrane with the highest IEC value will be the one exhibiting the higher protonic conductivity, since the IEC represents the quantity of ionizable groups that are responsible for the protonic conductivity of the membranes, as will be discussed in detail in the following section. Furthermore, the IEC values are in accordance with the *WU* capacity confirming that the latter parameter is also deeply correlated to the phosphate group of the polyelectrolyte. A similar trend was observed for the nanocomposites composed of cross-linked PMOEP (i.e., diprotic acidic phosphate bearing polymer, which is the monofunctional version (one polymerizable double bond) of *bis*MEP) and BC, whose IEC values were 1.95 mmol g^{-1} and 3.38 mmol g^{-1} for the nanocomposites containing 22 wt % and 48 wt % of the phosphate containing polymer, respectively [21]. These values are comparable to that of commercial membranes such as Nafion[®] ($0.95\text{--}1.01 \text{ mmol g}^{-1}$, DuPont Co., Wilmington, DE, USA), fumasep[®] FKB and FKD ($1.2\text{--}1.4 \text{ mmol g}^{-1}$, FuMA-Tech GmbH, Bietigheim-Bissingen, Germany), and JCM-II ($1.8\text{--}2.9 \text{ mmol g}^{-1}$, Tingrun Co., Ltd., Beijing, China) [27].

Table 4. Water-uptake (*WU*) and ion exchange capacity (IEC) of the P(*bis*MEP)/BC nanocomposite membranes and the corresponding individual components.

Sample *	<i>WU</i> /%	IEC/ mmol g^{-1}
BC	121 ± 11	–
P(<i>bis</i> MEP)	–	3.5 ± 0.02
P(<i>bis</i> MEP)/BC_1	79 ± 6	1.1 ± 0.12
P(<i>bis</i> MEP)/BC_2	155 ± 8	3.0 ± 0.05

* See Table 1 for sample identification.

3.5. Protonic Conductivity

The protonic conductivity of the nanocomposite membranes was assessed in the in-plane configuration. Figure 7 shows the impedance spectra of the two membranes collected at $80 \text{ }^\circ\text{C}$ and two different RH (20% and 98%) and normalized to the maximum in Z' to facilitate comparison. The spectra are in all cases dominated by one single semicircle at high frequency, with an amplitude corresponding to the ohmic resistance (R) of the membrane, which was used to calculate the conductivity. At high humidity, the membrane resistance decreases substantially, giving rise to the onset of a second contribution at low frequency, which is ascribed to the electrode impedance (that varies under variable test signal amplitude [20]). The capacitance associated to the high frequency relaxation is mostly the stray capacitance (C_{stray} , ca. 20–30 pF) due to the platinum wires of the sample holder (see Reference [20], including electronic supplementary data, and Reference [23] for further details on the analysis of impedance data). In fact, the capacitance of the sample in the in-plane direction is much lower due to the small cross-sectional area determined essentially by the thickness of the membrane ($C_{\text{in-plane}} = \epsilon_0 \epsilon_r w \delta L_0^{-1}$, where ϵ_0 and ϵ_r are the vacuum and relative permittivities, respectively, of the membrane material, and w , δ and L_0 are the width, thickness and length of the membrane). The shift of the relaxation (peak) frequency (given by $\nu_0 = 2\pi(RC_{\text{stray}})^{-1}$, assuming a parallel RC equivalent electric circuit) towards higher values, which is apparent in the spectrum of P(*bis*MEP)/BC_2 obtained at 98% RH, is due to the decrease in the membrane resistance, since C_{stray} remains unaltered by the external conditions. Therefore, for high humidity, the R corresponds to the Z' value at the minimum of Z'' observed on the transition between the high frequency semicircle and the low frequency electrode tale (Figure 7).

Figure 8 shows the Arrhenius plots of the in-plane protonic conductivity of both nanocomposite membranes (P(*bis*MEP)/BC_1 and P(*bis*MEP)/BC_2) measured under variable temperature ($30 \text{ }^\circ\text{C}$, $40 \text{ }^\circ\text{C}$, $60 \text{ }^\circ\text{C}$, $80 \text{ }^\circ\text{C}$ and $94 \text{ }^\circ\text{C}$) and RH (20%, 40%, 60%, 80% and 98%). The data clearly demonstrate the dependence of the protonic conductivity on temperature, RH and polyelectrolyte content, with RH as the parameter responsible for the most significant differences. In fact, the protonic conductivity of membrane P(*bis*MEP)/BC_1 increased 4 orders of magnitude from $35.8 \times 10^{-4} \text{ mS cm}^{-1}$ to 22.4 mS cm^{-1}

after raising the RH from 20% to almost saturated conditions (98%) at a temperature of 94 °C (Figure 8a). The impact of temperature is less pronounced with the protonic conductivity of membrane P(*bis*MEP)/BC_2 increasing less than one order of magnitude from 6.21 mS cm⁻¹ to 27.2 mS cm⁻¹ with the temperature augment from 30 °C to 80 °C at 98% RH (Figure 8b). Furthermore, the increase of the polyelectrolyte content from 21 wt % to 50 wt % (P(*bis*MEP)/BC_1 and P(*bis*MEP)/BC_2, respectively) promoted an increase of the protonic conductivity from 9.12 × 10⁻² mS cm⁻¹ to 23.6 × 10⁻² mS cm⁻¹ at 94 °C and 60% RH. This is a solid evidence, apart from the low conductivity of BC (ca. 60 μS cm⁻¹ at 94 °C, 98% RH) [20], that the protonic conductivity of these nanocomposite membranes is related with the acidic groups of P(*bis*MEP) and the resulting water-uptake ability of the nanocomposites (Table 4).

The protonic conductivities of the P(*bis*MEP)-based nanocomposite membranes are lower than those obtained for the cross-linked PMOEP/BC membranes prepared in our previous study ($\sigma > 100 \text{ mS cm}^{-1}$ at 98% RH and 20–94 °C, membrane with 48 wt % polyelectrolyte, IEC = 3.38 mmol g⁻¹) [21]. Since the IEC and the *WU* values of both membranes are similar, the higher conductivity of the cross-linked version must result from significant differences in the structure and/or distribution of the polyelectrolyte and the hydrated domains within the structure forming the ion transport paths. These factors are, however, difficult to access in detail given the predominately disordered molecular structure of the materials. Although the values of protonic conductivity of the P(*bis*MEP)-based nanocomposite membranes are lower than those usually found for Nafion® [46,47], the accomplished results may still be considered as promising in the present context.

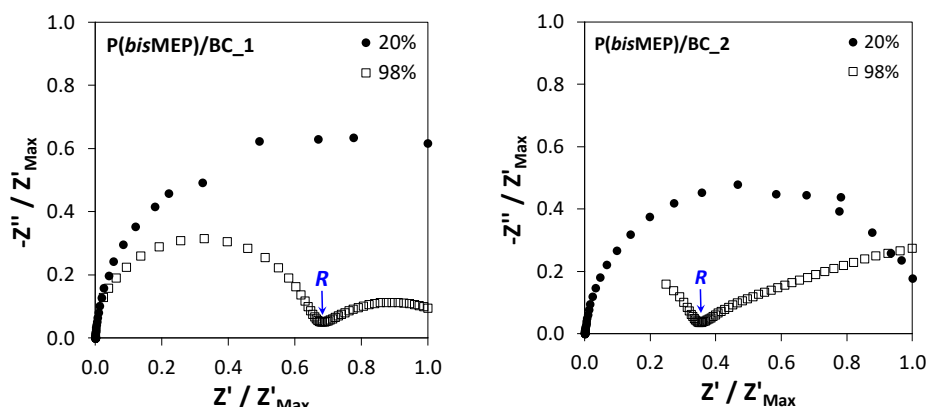


Figure 7. Nyquist plots of P(*bis*MEP)/BC_1 and P(*bis*MEP)/BC_2 collected at 80 °C and different RH (20 and 98%) (the values are normalized to the maximum in Z').

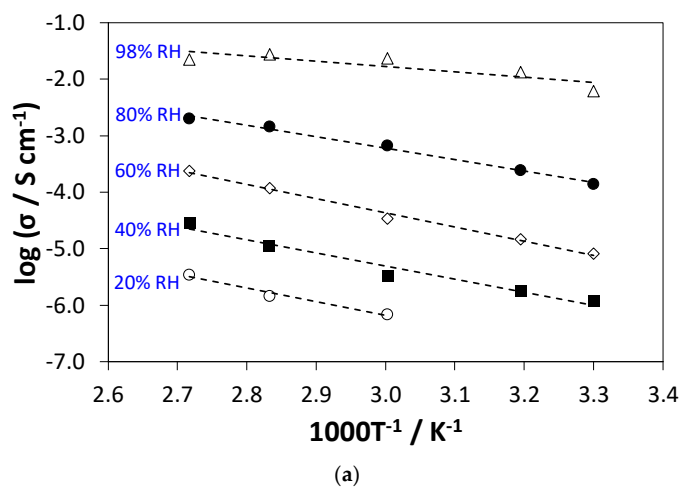


Figure 8. Cont.

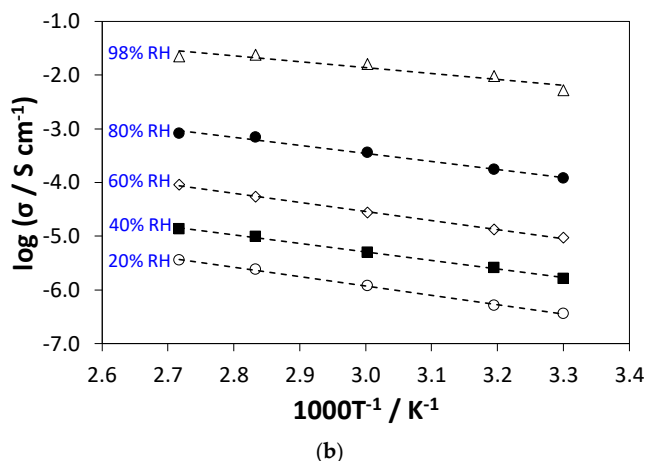


Figure 8. Arrhenius plot of the in-plane conductivity of the nanocomposite membranes P(*bis*MEP)/BC_1 (a) and P(*bis*MEP)/BC_2 (b) at different RH (relative humidity). The straight lines are linear fits to the Arrhenius model.

Regarding the temperature dependence, the conductivity data can be fitted by the Arrhenius equation: $\sigma = \sigma_0 \exp[-E_a/(RT)]$, where σ_0 is a pre-exponential term, E_a is the activation energy for proton transport, R is the gas constant and T is the absolute temperature. The estimated E_a values vary between 29–37 kJ mol⁻¹ for P(*bis*MEP)/BC_1 and 21–51 kJ mol⁻¹ for P(*bis*MEP)/BC_2, and this range of values is typically related with structural diffusion of protons as the leading transport mechanism. Data reported in literature for membranes composed of cross-linked PMOEP/BC [21] and poly(4-styrene sulfonic acid)/BC [20] display comparable E_a values. The activation energy is found to decrease with increasing humidity, particularly when reaching 98% RH. The behavior of P(*bis*MEP)/BC_1 is similar to that typically found for Nafion[®] [47].

4. Conclusions

The P(*bis*MEP)/BC-based nanocomposite systems studied here are a good example of proton-exchange BC-based nanocomposite membranes prepared through a simple and single-step methodology. The incorporation of a non-cross-linked polyelectrolyte onto the three-dimensional BC network originated membranes with thermal stability up to 195–205 °C, good mechanical performance (Young's modulus > 2 GPa), water-uptake ability (79–155%) and ion exchange capacity ($[H^+] = 1.1\text{--}3.0 \text{ mmol g}^{-1}$). Additionally, the mono-acidic phosphate moieties were responsible for the maximum protonic conductivity of ca. 0.03 S cm⁻¹ at 80 °C and 98% RH for the membrane containing 50 wt % of each component, and the temperature dependence of the conductivity followed an Arrhenius-type behavior typical of proton structural diffusion. The overall positive results of this study show that these polyelectrolyte membranes can be efficient proton-exchange membranes for application as proton separator materials in fuel cells or other devices such as sensors and actuators.

Author Contributions: C.V. and C.S.R.F. conceived, designed and supervised the experiments; C.V. wrote the paper; A.P.C.M. performed the experiments and analyzed the data; N.S. and F.M.L.F. carried out the conductivity measurements and analyzed the corresponding data, and also contributed to the tensile data interpretation; A.J.D.S. contributed to the structural, morphological, thermal and mechanical data interpretation; all authors participated in the critical revision of the paper.

Funding: This work was developed within the scope of the project CICECO-Aveiro Institute of Materials, POCI-01-0145-FEDER-007679 (FCT Ref. UID/CTM/50011/2013), and UniRCell POCI-01-0145-FEDER-016422 (Ref. SAICTPAC/0032/2015), financed by national funds through the FCT/MEC and when appropriate co-financed by FEDER under the PT2020 Partnership Agreement. The Portuguese Foundation for Science and Technology (FCT) is also acknowledged for the post-doctoral grant to C. Vilela (SFRH/BPD/84168/2012), doctoral grant to N. Sousa (SFRH/BD/89670/2012), and research contracts under Investigador FCT to C.S.R. Freire (IF/01407/2012) and F.M.L. Figueiredo (IF/01174/2013).

Conflicts of Interest: The authors declare no conflict of interest.

References

1. Junter, G.-A.; Lebrun, L. Cellulose-based virus-retentive filters: A review. *Rev. Environ. Sci. Biotechnol.* **2017**, *16*, 455–489. [[CrossRef](#)]
2. Kargarzadeh, H.; Mariano, M.; Gopakumar, D.; Ahmad, I.; Thomas, S.; Dufresne, A.; Huang, J.; Lin, N. Advances in cellulose nanomaterials. *Cellulose* **2018**, *25*, 2151–2189. [[CrossRef](#)]
3. Yang, J.; Li, J. Self-assembled cellulose materials for biomedicine: A review. *Carbohydr. Polym.* **2018**, *181*, 264–274. [[CrossRef](#)] [[PubMed](#)]
4. Figueiredo, A.R.P.; Vilela, C.; Neto, C.P.; Silvestre, A.J.D.; Freire, C.S.R. Bacterial Cellulose-Based Nanocomposites: Roadmap for Innovative Materials. In *Nanocellulose Polymer Composites*; Thakur, V.K., Ed.; Scrivener Publishing LLC: Beverly, MA, USA, 2014; pp. 17–64.
5. Vilela, C.; Pinto, R.J.B.; Figueiredo, A.R.P.; Neto, C.P.; Silvestre, A.J.D.; Freire, C.S.R. Development and applications of cellulose nanofibers based polymer composites. In *Advanced Composite Materials: Properties and Applications*; Bafekrpour, E., Ed.; De Gruyter Open: Berlin, Germany, 2017; pp. 1–65.
6. Dufresne, A. Cellulose nanomaterials as green nanoreinforcements for polymer nanocomposites. *Philos. Trans. R. Soc. A* **2018**, *376*. [[CrossRef](#)] [[PubMed](#)]
7. Abitbol, T.; Rivkin, A.; Cao, Y.; Nevo, Y.; Abraham, E.; Ben-Shalom, T.; Lapidot, S.; Shoseyov, O. Nanocellulose, a tiny fiber with huge applications. *Curr. Opin. Biotechnol.* **2016**, *39*, 76–88. [[CrossRef](#)] [[PubMed](#)]
8. Vilela, C.; Engström, J.; Valente, B.F.A.; Jawerth, M.; Carlmark, A.; Freire, C.S.R. Exploiting poly(ϵ -caprolactone) and cellulose nanofibrils modified with latex nanoparticles for the development of biodegradable nanocomposites. *Polym. Compos.* **2018**. [[CrossRef](#)]
9. Islam, S.; Chen, L.; Sisler, J.; Tam, K.C. Cellulose Nanocrystal (CNC)—Inorganic Hybrid Systems: Synthesis, Properties and Applications. *J. Mater. Chem. B* **2018**, *6*, 864–883. [[CrossRef](#)]
10. Reiniati, I.; Hrymak, A.N.; Margaritis, A. Recent developments in the production and applications of bacterial cellulose fibers and nanocrystals. *Crit. Rev. Biotechnol.* **2017**, *37*, 510–524. [[CrossRef](#)] [[PubMed](#)]
11. Moniri, M.; Moghaddam, A.B.; Azizi, S.; Rahim, R.A.; Ariff, A.B.; Saad, W.Z.; Navaderi, M.; Mohamad, R. Production and Status of Bacterial Cellulose in Biomedical Engineering. *Nanomaterials* **2017**, *7*. [[CrossRef](#)]
12. Greca, L.G.; Lehtonen, J.; Tardy, B.L.; Guo, J.; Rojas, O.J. Biofabrication of multifunctional nanocellulosic 3D structures: A facile and customizable route. *Mater. Horiz.* **2018**. [[CrossRef](#)]
13. Evans, B.R.; O'Neill, H.M.; Malyvanh, V.P.; Lee, I.; Woodward, J. Palladium-bacterial cellulose membranes for fuel cells. *Biosens. Bioelectron.* **2003**, *18*, 917–923. [[CrossRef](#)]
14. Yang, J.; Sun, D.; Li, J.; Yang, X.; Yu, J.; Hao, Q.; Liu, W.; Liu, J.; Zou, Z.; Gu, J. In situ deposition of platinum nanoparticles on bacterial cellulose membranes and evaluation of PEM fuel cell performance. *Electrochim. Acta* **2009**, *54*, 6300–6305. [[CrossRef](#)]
15. Yue, L.; Zheng, Y.; Xie, Y.; Liu, S.; Guo, S.; Yang, B.; Tang, T. Preparation of a carboxymethylated bacterial cellulose/polyaniline composite gel membrane and its characterization. *RSC Adv.* **2016**, *6*, 68599–68605. [[CrossRef](#)]
16. Yue, L.; Xie, Y.; Zheng, Y.; He, W.; Guo, S.; Sun, Y.; Zhang, T.; Liu, S. Sulfonated bacterial cellulose/polyaniline composite membrane for use as gel polymer electrolyte. *Compos. Sci. Technol.* **2017**, *145*, 122–131. [[CrossRef](#)]
17. Rogalsky, S.; Bardeau, J.F.; Makhno, S.; Babkina, N.; Tarasyuk, O.; Cherniavska, T.; Orlovska, I.; Kozyrovska, N.; Brovko, O. New proton conducting membrane based on bacterial cellulose/polyaniline nanocomposite film impregnated with guanidinium-based ionic liquid. *Polymer* **2018**, *142*, 183–195. [[CrossRef](#)]
18. Jiang, G.; Qiao, J.; Hong, F. Application of phosphoric acid and phytic acid-doped bacterial cellulose as novel proton-conducting membranes to PEMFC. *Int. J. Hydrogen Energy* **2012**, *37*, 9182–9192. [[CrossRef](#)]
19. Lin, C.W.; Liang, S.S.; Chen, S.W.; Lai, J.T. Sorption and transport properties of 2-acrylamido-2-methyl-1-propanesulfonic acid-grafted bacterial cellulose membranes for fuel cell application. *J. Power Sources* **2013**, *232*, 297–305. [[CrossRef](#)]

20. Gadim, T.D.O.; Figueiredo, A.G.P.R.; Rosero-Navarro, N.C.; Vilela, C.; Gamelas, J.A.F.; Barros-Timmons, A.; Neto, C.P.; Silvestre, A.J.D.; Freire, C.S.R.; Figueiredo, F.M.L. Nanostructured bacterial cellulose-poly(4-styrene sulfonic acid) composite membranes with high storage modulus and protonic conductivity. *ACS Appl. Mater. Interfaces* **2014**, *6*, 7864–7875. [[CrossRef](#)] [[PubMed](#)]
21. Vilela, C.; Gadim, T.D.O.; Silvestre, A.J.D.; Freire, C.S.R.; Figueiredo, F.M.L. Nanocellulose/poly(methacryloyloxyethyl phosphate) composites as proton separator materials. *Cellulose* **2016**, *23*, 3677–3689. [[CrossRef](#)]
22. Gadim, T.D.O.; Vilela, C.; Loureiro, F.J.A.; Silvestre, A.J.D.; Freire, C.S.R.; Figueiredo, F.M.L. Nafion® and nanocellulose: A partnership for greener polymer electrolyte membranes. *Ind. Crops Prod.* **2016**, *93*, 212–218. [[CrossRef](#)]
23. Gadim, T.D.O.; Loureiro, F.J.A.; Vilela, C.; Rosero-Navarro, N.; Silvestre, A.J.D.; Freire, C.S.R.; Figueiredo, F.M.L. Protonic conductivity and fuel cell tests of nanocomposite membranes based on bacterial cellulose. *Electrochim. Acta* **2017**, *233*, 52–61. [[CrossRef](#)]
24. Vilela, C.; Sousa, N.; Pinto, R.J.B.; Silvestre, A.J.D.; Figueiredo, F.M.L.; Freire, C.S.R. Exploiting poly(ionic liquids) and nanocellulose for the development of bio-based anion-exchange membranes. *Biomass Bioenergy* **2017**, *100*, 116–125. [[CrossRef](#)]
25. Jiang, G.; Zhang, J.; Qiao, J.; Jiang, Y.; Zarrin, H.; Chen, Z.; Hong, F. Bacterial nanocellulose/Nafion composite membranes for low temperature polymer electrolyte fuel cells. *J. Power Sources* **2015**, *273*, 697–706. [[CrossRef](#)]
26. Sharaf, O.Z.; Orhan, M.F. An overview of fuel cell technology: Fundamentals and applications. *Renew. Sustain. Energy Rev.* **2014**, *32*, 810–853. [[CrossRef](#)]
27. Ran, J.; Wu, L.; He, Y.; Yang, Z.; Wang, Y.; Jiang, C.; Ge, L.; Bakangura, E.; Xu, T. Ion exchange membranes: New developments and applications. *J. Membr. Sci.* **2017**, *522*, 267–291. [[CrossRef](#)]
28. Trovatti, E.; Serafim, L.S.; Freire, C.S.R.; Silvestre, A.J.D.; Neto, C.P. Gluconacetobacter sacchari: An efficient bacterial cellulose cell-factory. *Carbohydr. Polym.* **2011**, *86*, 1417–1420. [[CrossRef](#)]
29. Schuster, M.; Rager, T.; Noda, A.; Kreuer, K.D.; Maier, J. About the choice of the protogenic group in PEM separator materials for intermediate temperature, low humidity operation: A critical comparison of sulfonic acid, phosphonic acid and imidazole functionalized model compounds. *Fuel Cells* **2005**, *5*, 355–365. [[CrossRef](#)]
30. Chen, X.; Tolley, H.D.; Lee, M.L. Polymeric cation-exchange monolithic columns containing phosphoric acid functional groups for capillary liquid chromatography of peptides and proteins. *J. Chromatogr. A* **2010**, *1217*, 3844–3854. [[CrossRef](#)] [[PubMed](#)]
31. Chavan, V.; Agarwal, C.; Shinde, R.N. Phosphate barrier on pore-filled cation-exchange membrane for blocking complexing ions in presence of non-complexing ions. *Appl. Surf. Sci.* **2018**, *443*, 535–543. [[CrossRef](#)]
32. Jang, J.; Jeong, Y.K. Synthesis and flame-retardancy of UV-curable methacryloyloxy ethyl phosphates. *Fibers Polym.* **2008**, *9*, 667–673. [[CrossRef](#)]
33. Pecoraro, E.; Manzani, D.; Messaddeq, Y.; Ribeiro, S.J.L. Bacterial Cellulose from Gluconacetobacter xylinus: Preparation, Properties and Applications. In *Monomers, Polymers and Composites from Renewable Resources*; Belgacem, M.N., Gandini, A., Eds.; Elsevier: Amsterdam, The Netherlands, 2008; pp. 369–383.
34. Bellamy, L.J. *The Infrared Spectra of Complex Molecules*, 3rd ed.; Chapman and Hall, Ltd.: London, UK, 1975; ISBN 0412138506.
35. Lacerda, P.S.S.; Barros-Timmons, A.M.M.V.; Freire, C.S.R.; Silvestre, A.J.D.; Neto, C.P. Nanostructured Composites Obtained by ATRP Sleaving of Bacterial Cellulose Nanofibers with Acrylate Polymers. *Biomacromolecules* **2013**, *14*, 2063–2073. [[CrossRef](#)] [[PubMed](#)]
36. French, A.D. Idealized powder diffraction patterns for cellulose polymorphs. *Cellulose* **2014**, *21*, 885–896. [[CrossRef](#)]
37. Nishiyama, Y.; Sugiyama, J.; Chanzy, H.; Langan, P. Crystal structure and hydrogen bonding system in cellulose I α from synchrotron x-ray and neutron fiber diffraction. *J. Am. Chem. Soc.* **2003**, *125*, 14300–14306. [[CrossRef](#)] [[PubMed](#)]
38. Dadsetan, M.; Giuliani, M.; Wanivenhaus, F.; Brett Runge, M.; Charlesworth, J.E.; Yaszemski, M.J. Incorporation of phosphate group modulates bone cell attachment and differentiation on oligo(polyethylene glycol) fumarate hydrogel. *Acta Biomater.* **2012**, *8*, 1430–1439. [[CrossRef](#)] [[PubMed](#)]
39. Wang, S.; Liu, Q.; Luo, Z.; Wen, L.; Cen, K. Mechanism study on cellulose pyrolysis using thermogravimetric analysis coupled with infrared spectroscopy. *Front. Energy Power Eng. China* **2007**, *1*, 413–419. [[CrossRef](#)]

40. Du, L.; Jana, S.C. Highly conductive epoxy/graphite composites for bipolar plates in proton exchange membrane fuel cells. *J. Power Sources* **2007**, *172*, 734–741. [[CrossRef](#)]
41. Wang, S.; Jiang, F.; Xu, X.; Kuang, Y.; Fu, K.; Hitz, E.; Hu, L. Super-strong, super-stiff macrofibers with aligned, long bacterial cellulose nanofibers. *Adv. Mater.* **2017**, *29*, 29. [[CrossRef](#)] [[PubMed](#)]
42. DuPont™ Nafion®PFSA Membranes. Available online: https://www.chemours.com/Nafion/en_US/assets/downloads/nafion-extrusion-cast-membranes-product-information.pdf (accessed on 15 June 2018).
43. Tanpichai, S.; Quero, F.; Nogi, M.; Yano, H.; Young, R.J.; Lindström, T.; Sampson, W.W.; Eichhorn, S.J. Effective Young's modulus of bacterial and microfibrillated cellulose fibrils in fibrous networks. *Biomacromolecules* **2012**, *13*, 1340–1349. [[CrossRef](#)] [[PubMed](#)]
44. Peura, M.; Grotkopp, I.; Lemke, H.; Vikkula, A.; Laine, J.; Müller, M.; Serimaa, R. Negative poisson ratio of crystalline cellulose in kraft cooked Norway spruce. *Biomacromolecules* **2006**, *7*, 1521–1528. [[CrossRef](#)] [[PubMed](#)]
45. Hervy, M.; Santmarti, A.; Lahtinen, P.; Tammelin, T.; Lee, K.Y. Sample geometry dependency on the measured tensile properties of cellulose nanopapers. *Mater. Des.* **2017**, *121*, 421–429. [[CrossRef](#)]
46. Rosero-Navarro, N.C.; Domingues, E.M.; Sousa, N.; Ferreira, P.; Figueiredo, F.M. Protonic conductivity and viscoelastic behaviour of Nafion®membranes with periodic mesoporous organosilica fillers. *Int. J. Hydrogen Energy* **2014**, *39*, 5338–5349. [[CrossRef](#)]
47. Rosero-Navarro, N.C.; Domingues, E.M.; Sousa, N.; Ferreira, P.; Figueiredo, F.M.L. Meso-structured organosilicas as fillers for Nafion®membranes. *Solid State Ion.* **2014**, *262*, 324–327. [[CrossRef](#)]



© 2018 by the authors. Licensee MDPI, Basel, Switzerland. This article is an open access article distributed under the terms and conditions of the Creative Commons Attribution (CC BY) license (<http://creativecommons.org/licenses/by/4.0/>).